



# Purification of hydrogen from carbon monoxide for fuel cell application over modified mesoporous CuO–CeO<sub>2</sub> catalysts

Jing Li<sup>a</sup>, Yuxi Han<sup>a</sup>, Yihan Zhu<sup>b</sup>, Renxian Zhou<sup>a,\*</sup>

<sup>a</sup> Institute of Catalysis, Zhejiang University, Hangzhou 310028, PR China

<sup>b</sup> Division of Chemical and Life Sciences and Engineering, King Abdullah University of Science and Technology, Thuwal 23955–6900, Saudi Arabia

## ARTICLE INFO

### Article history:

Received 30 May 2011

Received in revised form 26 July 2011

Accepted 12 August 2011

Available online 19 August 2011

### Keywords:

CuO–CeO<sub>2</sub>

Transition metals

CO selective oxidation

Cu<sup>+</sup>

Oxygen vacancies

## ABSTRACT

Selective oxidation of CO in H<sub>2</sub>-rich streams was carried out over a series of CuO–CeO<sub>2</sub> catalysts doped by different transition metals (Mn, Fe, Ni, Ti, Co and Cr). The effect of the dopants on the structure and catalytic properties of CuO–CeO<sub>2</sub> catalysts was investigated by N<sub>2</sub> adsorption/desorption, X-ray diffraction (XRD), H<sub>2</sub> temperature-programmed reduction (H<sub>2</sub>-TPR), X-ray photoelectron spectroscopy (XPS), Raman spectra and in situ diffuse reflectance infrared Fourier transform spectroscopy (DRIFTS) techniques. The results show that the addition of Mn and Fe plays a beneficial role in extending the low-temperature catalytic activity of CuO–CeO<sub>2</sub> catalysts, whereas the introduction of Cr and Co leads to a negative effect on the catalytic activity and resistance against CO<sub>2</sub> and H<sub>2</sub>O. The superior catalytic performance of CuO–CeO<sub>2</sub> catalysts with Mn and Fe doping originates from the enhanced interaction between copper and ceria, owing to the formation of more Cu<sup>+</sup> and oxygen vacancies in the solid solution framework. While the poor catalytic activity of the Co doped counterpart is mainly ascribed to the substitution of introduced cobalt ions for copper ions in ceria lattice, resulting in the segregation of copper ions from the ceria lattice and the consequent aggregation of copper species on the ceria surface. The doping of Cr into CuO–CeO<sub>2</sub> structure remarkably weakens the interaction between copper and ceria, which decreases the reducibility of copper species and inhibits the formation of Cu<sup>+</sup>. It accounts for the lowest catalytic activity.

© 2011 Elsevier B.V. All rights reserved.

## 1. Introduction

Hydrogen, as an ideal fuel for polymer electrolyte membrane fuel cells (PEMFCs), has been produced from the steam reforming or autothermal reforming (such as methanol, ethanol, natural gas and gasoline) processes followed by the water–gas shift (WGS) reaction [1]. However, the produced H<sub>2</sub>-rich gases from the WGS reaction generally contain 0.5–2.0 vol.% of CO, which can poison the Pt-based anode in the PEMFCs [2]. Therefore, purification of the H<sub>2</sub>-rich gases is of vital importance, which aims to lower the CO concentration to less than 100 ppm as a tolerance of PEMFCs [3,4]. Currently, efficient strategies for CO removal include pressure swing adsorption, Pd or Pt-alloy membrane separation, CO methanation and selective oxidation [5–7]. The selective oxidation of CO is considered as one of the most direct and cheap methods to achieve the CO tolerance. Ideal catalyst designed for this target should have high activity and selectivity as well as good thermal stability. The most efficient catalytic systems are noble metals (Pt, Ru, Pd, Rh) [8–10], gold [11–13] and transition metal oxides catalysts [2,14–16]. Although noble metals and gold catalysts are active for the selective oxidation of CO,

higher reaction temperature (about 150–300 °C) for noble metal catalysts and poor selectivity for gold catalysts as well as their high cost greatly limit their application. CuO–CeO<sub>2</sub> based catalysts open a new era eliminating CO in H<sub>2</sub>-rich streams due to their excellent catalytic performance and low cost [6,15,17–26].

Regarding to the superior catalytic performance of CuO–CeO<sub>2</sub> catalysts, the interaction between copper and ceria is important. Ceria itself has high oxygen storage capability (OSC) as well as the ability of stabilization of the dispersed metal cation species. The interaction between copper species and ceria, by means of the formation of interfacial active centers between CuO<sub>x</sub> and CeO<sub>2</sub> domains [27], leads to a stronger redox property and high catalytic activity. Recently, studies have shown that the introduction of a third or fourth element could readily improve the OSC of the support, redox property, thermal resistance or the interaction between active component and support. Chen et al. [28,29] reported that doping an appropriate amount of zirconium into CeO<sub>2</sub> increased the mobility of lattice oxygen while the incorporation of aluminum increased the dispersion of Ce<sub>x</sub>Zr<sub>1-x</sub>O<sub>2</sub>, which makes a 7%CuO/Ce<sub>0.9</sub>Zr<sub>0.1</sub>O<sub>2</sub>–Al<sub>2</sub>O<sub>3</sub> (20%) catalyst to have a better selectivity than the 5% Pt/Al<sub>2</sub>O<sub>3</sub> catalyst. Huang and Kung [30] modified ceria by doping with gadolinia or yttria and found that the formation of extrinsic oxygen vacancies because the Ga doping increased the oxygen ionic conductivity of ceria support. Chen et al. [31]

\* Corresponding author. Tel.: +86 571 88273290; fax: +86 571 88273283.  
E-mail address: [zhourenxian@zju.edu.cn](mailto:zhourenxian@zju.edu.cn) (R. Zhou).

investigated that the addition of MgO promoted the dispersion of CuO and the incorporation of copper ions into ceria lattice. Jung et al. [32] found that there was a strong interaction between doped Pt and CuO–CeO<sub>2</sub> catalyst, which inhibits the phase separation of copper. Wu et al. [33] suggested that the doping of Ti in ceria not only enhanced the surface area by decreasing the particle size of the support but also promoted the dispersion of active copper species; moreover, owing to the doping of Ti a stronger interaction between CuO and the support was achieved, which was a major reason for the high catalytic activity of CuO/Ce<sub>0.8</sub>Ti<sub>0.2</sub>O<sub>2</sub>.

The dopant cations with ionic radius and electronegativity approximate to those of Ce<sup>4+</sup> are considered as the most efficient modifiers for tuning the structural and chemical properties of CeO<sub>2</sub> [34]. The introduction of dopant with multiple oxidation states also facilitates the excellent redox properties and fasts electron transfer rate [35]. Concerning the above facts, we synthesized a series of CuO–CeO<sub>2</sub> catalysts doped with different transition metals (Mn, Fe, Ni, Ti, Co, Cr) by hydrothermal method. The doping effect of transition metals in the CuO–CeO<sub>2</sub> catalytic system was evaluated by selective oxidation of CO in H<sub>2</sub>-rich streams, which were further characterized by N<sub>2</sub> adsorption/desorption, XRD, H<sub>2</sub>-TPR, XPS, Raman and in situ DRIFTS techniques.

## 2. Experimental

### 2.1. Catalyst synthesis

Doped CuO–CeO<sub>2</sub> mixed oxide catalysts were prepared by hydrothermal method. Nitrate salts of Ce(NO<sub>3</sub>)<sub>3</sub>·6H<sub>2</sub>O, Cu(NO<sub>3</sub>)<sub>2</sub>·3H<sub>2</sub>O, and M(NO<sub>3</sub>)<sub>x</sub> (M = Mn, Fe, Ni, Ti, Co, Cr) as well as cetyltrimethyl ammonium bromide (CTAB; CTAB:Ce molar ratio was 1:1) were dissolved in ethanol with fixed copper content (Cu/(CuO + CeO<sub>2</sub>)) wt% was always 5.0 wt% and modifier content (the molar ratio of M to Cu was 1:5). NH<sub>3</sub>·H<sub>2</sub>O was added dropwise to the mixed ethanol solution to adjust the pH value to 9.0. And then, the obtained slurry was aged at 100 °C for 1 h in a stainless steel autoclave. The precipitate was separated by filtration, dried at 110 °C and then calcined at 500 °C for 2 h in air. The obtained CuO–CeO<sub>2</sub> catalyst and CuO–CeO<sub>2</sub> catalysts doped with Mn, Fe, Ni, Ti, Co and Cr were labeled as CuC, CuC–Mn, CuC–Fe, CuC–Ni, CuC–Ti, CuC–Co and CuC–Cr, respectively.

### 2.2. Catalytic performance tests

The catalytic performance tests for selective oxidation of CO in H<sub>2</sub>-rich streams were carried out in a fixed-bed micro-reactor (quartz glass, i.d. = 6 mm) at atmospheric pressure. 100 mg of catalyst was used in the test, which was diluted with inert  $\alpha$ -alumina particles of the same mesh (60–80) with a mass ratio of 2:1. Prior to reactions, the samples were pretreated in oxygen at 150 °C for 0.5 h. The composition of reactant gas was 1.0% CO (by volume, hereinafter), 1.0% O<sub>2</sub>, 50% H<sub>2</sub>, 15% CO<sub>2</sub> (when used), 7.5% H<sub>2</sub>O (when used) and Ar in balance. The total flow rate was 100 ml/min, and the space velocity was 60,000 ml g<sup>−1</sup> h<sup>−1</sup>.

The effluent gases were measured by an on-line gas chromatograph equipped with a thermal conductivity detector (TCD) and a flame ionization detector (FID). H<sub>2</sub> and O<sub>2</sub> were separated by a carbon molecular sieve (TDX-01) column and detected by TCD. CO and CO<sub>2</sub> were separated by a carbon molecular sieve (TDX-01) column, and converted to methane by a methanation reactor and analyzed by FID. The detection limit of FID for CO is 3 ppm.

Taking CO<sub>2</sub> in the feedstock into consideration, the conversion can be calculated as follows:

$$\text{CO conversion} = \frac{[\text{CO}]_{\text{in}} - [\text{CO}]_{\text{out}}}{[\text{CO}]_{\text{in}}} \times 100(\%)$$

**Table 1**

Characteristics of CuO–CeO<sub>2</sub> catalysts doped with transition metals.

Catalysts	Lattice parameter (nm)	Crystallite size (nm)	S <sub>BET</sub> (m <sup>2</sup> g <sup>−1</sup> )	T <sub>50</sub> (°C)
CuC	0.5413	8.4	52	82
CuC–Mn	0.5410	8.7	68	74
CuC–Fe	0.5407	8.5	65	51
CuC–Ni	0.5413	12.1	33	82
CuC–Ti	0.5409	8.0	78	77
CuC–Co	0.5411	15.5	29	85
CuC–Cr	0.5412	9.1	61	93

The selectivity was evaluated from the oxygen mass balance as follows:

$$\text{Selectivity} = \frac{0.5([\text{CO}]_{\text{in}} - [\text{CO}]_{\text{out}})}{[\text{O}_2]_{\text{in}} - [\text{O}_2]_{\text{out}}} \times 100(\%)$$

Where “in” and “out” is the mean inlet and outlet gaseous stream, respectively.

### 2.3. Catalyst structure characterization

Nitrogen adsorption and desorption isotherms were determined on a Tristar II 3020 apparatus at −195.8 °C. The specific surface areas were calculated by the BET method.

Powder X-ray diffraction (XRD) patterns were recorded on a Rigaku D/Max 2550 PC powder diffractometer using nickel-filtered CuK $\alpha$  radiation in the range of 20° ≤ 2 $\theta$  ≤ 80°. The X-ray tube was operated at 40 kV and 300 mA. The average crystallite size was estimated from the line broadening with the Scherrer formula.

H<sub>2</sub> temperature-programmed reduction (H<sub>2</sub>-TPR) was carried out in a quartz fixed-bed micro-reactor. In each run, 50 mg of catalyst was used, the reduction gas mixture was 5 vol.% H<sub>2</sub>/Ar (40 mL min<sup>−1</sup>), the heating rate was 10 °C min<sup>−1</sup>. The consumption of H<sub>2</sub> during the reduction was measured by TCD.

X-ray photoelectron spectroscopy (XPS) measurements were recorded with a PHI5000c spectrometer at 1486.6 eV and 12.5 kV using Al K $\alpha$  radiation.

UV–Raman spectra were recorded on a UV–HR Raman spectrograph with a He–Gd laser of 325 nm excitation wavelength. The spectral resolution was 4 cm<sup>−1</sup>, and the spectra acquisition consisted of 2 accumulations of 30 s for each sample.

In situ diffuse reflectance infra-red Fourier transform spectroscopy (DRIFTS) data were collected with a Nicolet 6700 apparatus equipped with an MCT detector. A diffuse reflection infrared cell, equipped with temperature controlled parts and CaF<sub>2</sub> window, was connected with a vacuum apparatus. Spectra were averaged over 32 scans with a resolution of 4 cm<sup>−1</sup>. Prior to infrared experiment, the sample was pretreated with 10% O<sub>2</sub> at 300 °C for 0.5 h and then cooled to 25 °C in order to remove the contaminants from the catalyst surface. The composition of feed stream was 1% CO, 1% O<sub>2</sub>, 50% H<sub>2</sub> and Ar in balance. The deconvolution and integrated area of peaks was carried out by the Gaussian profiles.

## 3. Results and discussion

### 3.1. Catalytic performance of the catalysts

Fig. 1 presents the CO conversion and O<sub>2</sub> selectivity for CO selective oxidation in H<sub>2</sub>-rich streams on CuO–CeO<sub>2</sub> catalysts doped by different transition metals (Mn, Fe, Ni, Ti, Co, Cr) in the basic reaction streams. The temperature of 50% CO conversion (T<sub>50</sub>) is listed in Table 1. It is clear that the addition of Mn and Fe plays a beneficial role in extending the low-temperature catalytic activity of CuO–CeO<sub>2</sub> catalysts, while the doping of Co and Cr leads

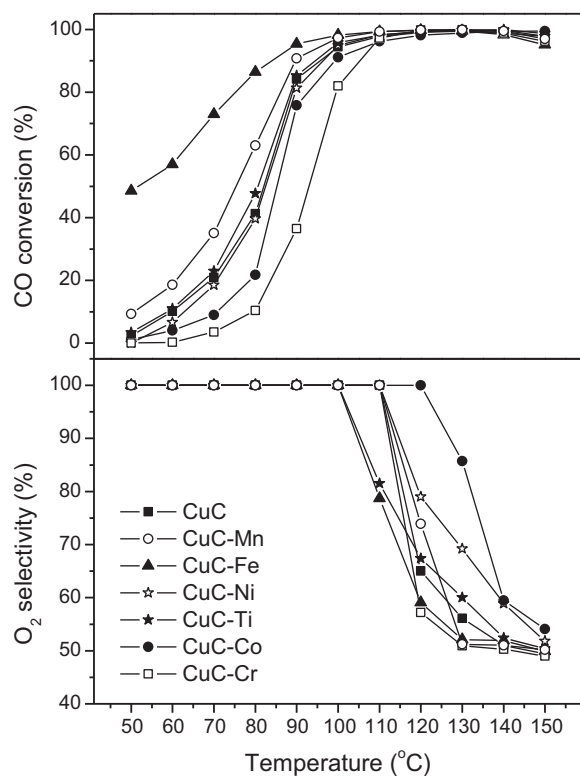


**Fig. 1.** Temperature-programmed reaction curves of the CO selective oxidation in the basic  $H_2$ -rich streams over  $CuO-CeO_2$  catalysts doped with transition metals. Reaction conditions: 1%  $CO$ , 1%  $O_2$ , 50%  $H_2$ , and balanced  $Ar$ ;  $SV = 60,000 \text{ ml g}^{-1} \text{ h}^{-1}$ .

to a negative effect.  $CuC-Mn$  catalyst exhibits the widest temperature window (the temperature range of  $CO$  conversions up to 99.0%), about  $40^\circ C$ , from 110 to  $140^\circ C$ .  $CuC-Fe$  catalyst has the best low-temperature activity;  $T_{50}$  is only  $51^\circ C$ , which is much lower than that of  $CuC-Mn$  catalyst. In addition, doping  $Fe$  into  $CuO-CeO_2$  catalyst broadens the temperature window by  $30^\circ C$  ( $110-130^\circ C$ ) while  $CuC$  catalyst only has a  $20^\circ C$  wide window, from 120 to  $130^\circ C$ . On the contrary,  $CuC-Cr$  catalyst shows the lowest low-temperature activity and  $O_2$  selectivity for  $CO$  selective oxidation,  $T_{50}$  is up to  $93^\circ C$ .  $CuC-Co$  catalyst displays a lower low-temperature activity and a temperature window shifting to higher temperature ( $140-150^\circ C$ ); however, it attains the best selectivity of  $O_2-CO$  oxidation reaction (selectivity of  $O_2-CO$  oxidation reaction for  $CuC-Co$  catalyst still maintains 100% at  $120^\circ C$ ). Besides, the doping of  $Ni$  and  $Ti$  promotes the catalytic activity to a certain extent, according to the wider temperature windows of  $30^\circ C$ , from 120 to  $140^\circ C$  for both catalysts. Therefore, the order of catalytic activity of  $CuO-CeO_2$  catalysts modified by different transition metals for  $CO$  selective oxidation is as follows:  $CuC-Mn \approx CuC-Fe > CuC-Ti > CuC-Ni > CuC > CuC-Co > CuC-Cr$ .

To further observe the influence of doping transition metals on the catalytic performance for selective oxidation of  $CO$  in  $H_2$ -rich streams, 15 vol.%  $CO_2$  and 7.5 vol.%  $H_2O$  are introduced into the basic reaction streams to investigate the deactivation of catalysts and the results are shown in Fig. 2. Obviously, the presence of  $CO_2$  and  $H_2O$  causes a sharp decrease in the  $CO$  oxidative activity and narrows the temperature window for achieving a  $CO$  concentration below 100 ppm (i.e.  $CO$  conversion is greater than 99.0%), due to the blocking effect of adsorbed molecular water and the accumulation of carbonate species [36,37].  $CuC$  catalyst completely loses its activity under the reaction streams with  $CO_2$  and  $H_2O$ .  $CuC-Mn$  and  $CuC-Ni$  catalysts still maintain  $20^\circ C$  wide window and  $CuC-Ti$  catalyst maintains  $10^\circ C$  wide window, indicating that the doping

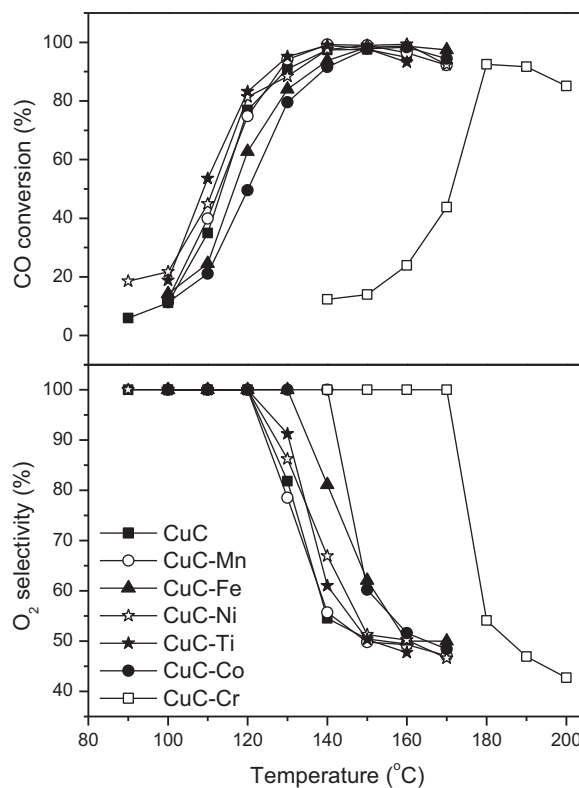


**Fig. 2.** Temperature-programmed reaction curves of the  $CO$  selective oxidation in  $H_2$ -rich streams over  $CuO-CeO_2$  catalysts doped with transition metals. Reaction conditions: 1%  $CO$ , 1%  $O_2$ , 15%  $CO_2$ , 7.5%  $H_2O$ , 50%  $H_2$ , and balanced  $Ar$ ;  $SV = 60,000 \text{ ml g}^{-1} \text{ h}^{-1}$ .

of  $Mn$ ,  $Ni$  and  $Ti$  enhances the resistance against  $CO_2$  and  $H_2O$  of  $CuO-CeO_2$  catalyst. However, the addition of  $Fe$ ,  $Cr$  or  $Co$  decreases the resistance against  $CO_2$  and  $H_2O$ . Additionally, it worth noticing that  $CuC-Cr$  catalyst suffers seriously from the deactivation by the presence of 15%  $CO_2$  and 7.5%  $H_2O$  in the reaction gas, according to that  $\Delta T_{50}$  ( $\Delta T_{50} = T_{50}$ , Fig. 2 –  $T_{50}$ , Fig. 1) is up to  $80^\circ C$  for  $CuC-Cr$  catalyst while those of other catalysts are only about  $30^\circ C$ . Besides,  $CuC-Cr$  catalyst still exhibits the best selectivity of  $O_2-CO$  oxidation reaction while other catalysts display the similar selectivity of  $O_2-CO$  oxidation reaction.

### 3.2. Characterization of catalysts

#### 3.2.1. $N_2$ adsorption measurements

The  $N_2$  adsorption/desorption isotherms and BJH pore size distribution curves of  $CuO-CeO_2$  catalysts doped with transition metals are shown in Fig. 3 and the corresponding values of the specific area calculated according to the BET method are listed in Table 1. As shown in Fig. 3, all the catalysts exhibit a type IV isotherm and have a mesoporous structure. The pore size distribution of all the catalysts except for  $CuC-Cr$  sample are about 2.0–5.0 nm, and  $CuC-Mn$  catalyst has the most uniform pore size. Considering their respective catalytic performance, a more ordered and narrower distribution of mesopores favors the catalytic performance of  $CuO-CeO_2$  catalyst. However, the distribution pores of  $CuC-Cr$  catalyst is about 5.0–14.0 nm. The larger pore size and wider pore distribution with the smaller pore volume in the  $CuC-Cr$  catalyst may be one reason for the poor catalytic activity of  $CO$  selective oxidation. Furthermore, as reported in literature [38], the closure point of hysteresis loop for the type IV isotherm is closely related to the size of pores. At low relative pressure, the larger the pore size, the higher the pressure of closure point. That is why the closure

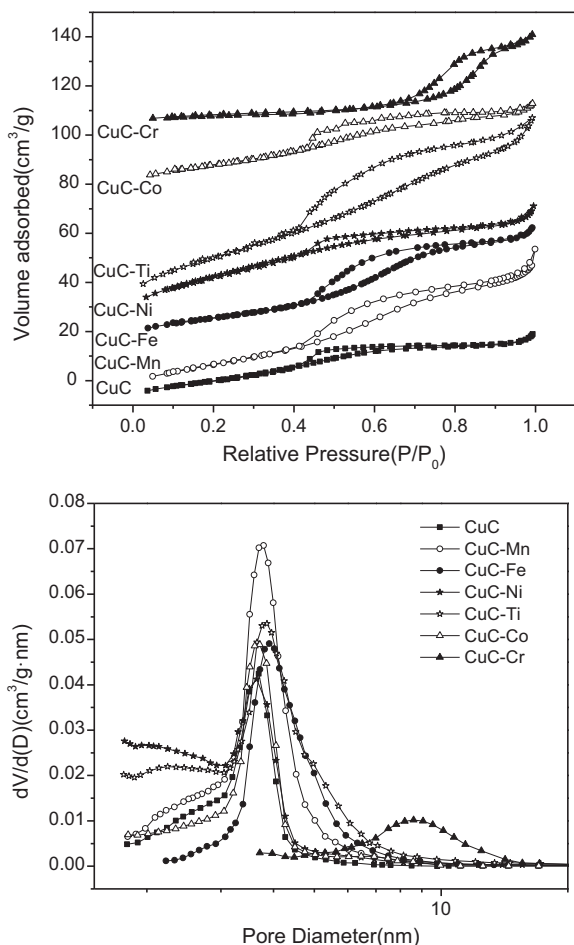


Fig. 3. N<sub>2</sub> adsorption/desorption isotherms and BJH pore-size distribution CuO–CeO<sub>2</sub> catalysts doped with transition metals.

point of hysteresis loop of CuC–Cr catalyst appears at  $P/P_0 = 0.50$  while those of other catalysts appear at about  $P/P_0 = 0.42$ . However, according to the results listed in Table 1, the BET specific area of CuC catalyst is not obviously changed due to the introduction of Mn, Fe, Ti, Ni, Cr and Co.

### 3.2.2. XRD

Fig. 4 shows the XRD patterns of CuO–CeO<sub>2</sub> catalysts doped with different transition metals and Table 1 lists the lattice parameter and corresponding crystallite size, which are calculated from the (111) plane ( $2\theta = \text{ca. } 28.7^\circ$ ) using Scherrer's equation. For all the samples, the diffraction peaks could be indexed to (111), (200), (220), (311), (222) and (400) reflections, corresponding to a face centered cubic fluorite structure of CeO<sub>2</sub>. No obvious diffraction lines, except for those of CuC–Ni catalyst, ascribed to dopants or their derivatives are detected, which means that the dopants highly disperse on the ceria surface or incorporate into the ceria lattice to form solid solution [5,39,40]. Some diffraction peaks of crystalline NiO at  $37.3^\circ$ ,  $43.2^\circ$  and  $62.8^\circ$  (PDF-ICDD 44-1159) are observed, indicating that the nickel oxide easily aggregates on the ceria surface. What is more, for CuC–Ni and CuC–Co catalysts, some diffraction peaks of crystalline CuO at  $35.6^\circ$  and  $38.7^\circ$  (PDF-ICDD 45-0937) are also observed, due to the aggregation of copper species on the surface of cerium oxide, which is caused by the doping of Ni or Co. As a result, the crystallite size of CuC–Ni and CuC–Co catalysts is much bigger than that of CuC catalyst. Big crystallite size and the aggregation of copper species on the surface of cerium oxide may be disadvantageous to

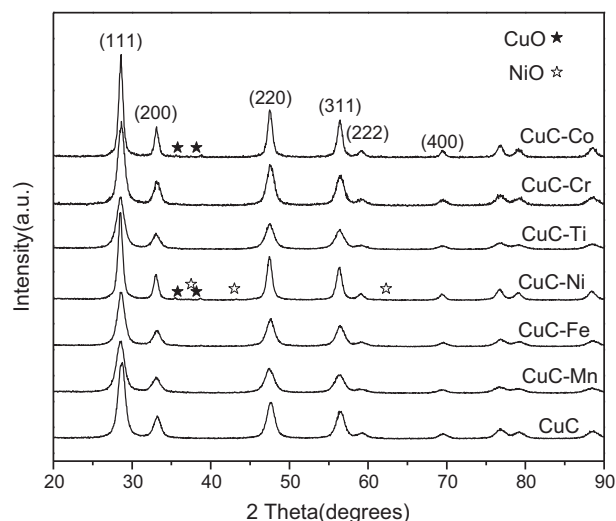


Fig. 4. Power XRD patterns of CuO–CeO<sub>2</sub> catalysts doped with transition metals.

the selective oxidation of CO in H<sub>2</sub>-rich streams [21]. Additionally, the lattice parameter of CeO<sub>2</sub> is obtained in Table 1 in the sequence of CuC–Fe < CuC–Ti < CuC–Mn < CuC–Co < CuC–Cr < CuC–Ni < CuC. Considering the smaller ionic radii of dopants than that of Ce<sup>4+</sup> [2,33,41–43], the decreased lattice parameter indicates that some of dopants and/or copper ions incorporate into the ceria lattice to form solid solution. Moreover, the lattice parameter of CuC–Mn, CuC–Fe and CuC–Ti catalysts is much smaller than that of CuC catalyst, suggesting that the additions of Mn, Fe and Ti favor the formation of more solid solution. According to the previous studies [2,44], the existence of solid solution signifies a stronger interaction between active components and ceria, which is favorable to the selective oxidation of CO in H<sub>2</sub>-rich streams.

### 3.2.3. H<sub>2</sub>-TPR

Fig. 5 shows the H<sub>2</sub>-TPR profiles of CuO–CeO<sub>2</sub> catalysts modified by different transition metals. For CuO–CeO<sub>2</sub> catalyst, three reduction peaks appear in its TPR profile (referred to  $\alpha$ ,  $\beta$  and  $\gamma$ ), which may be ascribed to the reduction of the copper species strongly and weakly interacting with the ceria as well as Cu<sup>+</sup> species [45]. Obviously, the reduction peaks shifts to lower temperatures by the presence of Fe, Ni and Co, suggesting that the introduction of these three metals promotes the reduction of CuO–CeO<sub>2</sub> at low

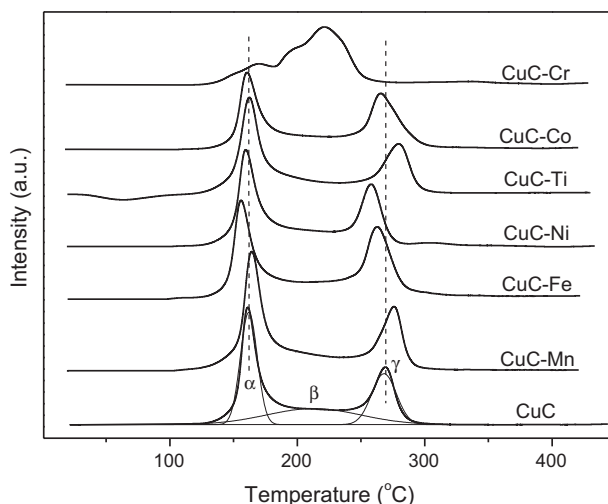


Fig. 5. H<sub>2</sub>-TPR profiles of CuO–CeO<sub>2</sub> catalysts doped with transition metals.



**Table 2**

Surface contents of Cu and M (M = Mn, Fe, Ni, Ti, Co, Cr) and surface atom ratios in the CuO–CeO<sub>2</sub> catalysts with transition metals derived by XPS.

Sample	Cu/(Cu + Ce + M) (at.%)	M/(Cu + Ce + M) (at.%)	M/Cu	Ce <sup>3+</sup> 3d <sub>5/2</sub> in Ce (%)
CuC	23.8	–	–	14.9
CuC–Mn	19.0	7.0	0.37	17.0
CuC–Fe	20.6	0.3	0.01	16.7
CuC–Ni	21.1	3.9	0.18	13.1
CuC–Ti	20.2	3.5	0.17	15.3
CuC–Co	24.9	1.7	0.07	12.4
CuC–Cr	20.5	5.1	0.24	11.9

temperature. The reducibility of copper species for the corresponding samples is on the order of CuC–Fe > CuC–Ni > CuC–Co > CuC. Moreover, CuC–Fe catalyst possesses the smallest CeO<sub>2</sub> lattice parameter, as revealed by the XRD results, indicating the onset of a strong interaction existing in copper, iron species and CeO<sub>2</sub> and the formation of a solid solution, where Ce–O bond is weakened and the interaction between the three components is enhanced. This may be contributed to the high catalytic activity of CuC–Fe catalyst at low temperatures. In addition, despite the slightly higher reduction temperatures than those of CuC catalyst, CuC–Mn catalyst also shows the outstanding reducibility for the higher intensity of  $\alpha$  peak than those of other samples. What is more, it is worth noticing that there is almost no reduction peak of  $\gamma$  appearing at the H<sub>2</sub> consumption profiles of CuC–Cr catalyst. The H<sub>2</sub> consumption profiles of CuC–Cr catalyst show a low intensity of  $\alpha$  peak and a wide and high intensity of  $\beta$  peak, indicating that the introduction of Cr weakens the strong interaction between copper species and the ceria. The weakened interaction between copper species and CeO<sub>2</sub> leads to a poor reducibility of copper species [4] and inhibits the formation of Cu<sup>+</sup> species [21,46], which is regarded as the main active centers of CO adsorption over the CuO–CeO<sub>2</sub> catalysts [29,36]. This may be the main reason for the worst catalytic activity of CuC–Cr catalyst for selective oxidation of CO in H<sub>2</sub>-rich streams.

### 3.2.4. XPS

XPS investigation was conducted to provide information on the surface contents and the oxidation states of copper and cerium in the mixed oxides. The surface element contents and atomic ratios obtained by XPS are listed in Table 2. For CuO–CeO<sub>2</sub> catalysts doped with different transition metals except for Co, the surface contents of Cu are lower than that of CuC catalyst, which indicates more copper ions incorporate into the ceria lattice to form solid solution. Moreover, only the surface M/Cu atomic ratio of CuC–Mn catalyst is much higher than the theoretical atomic ratio of 0.2, implying that the introduction of Mn mainly exists on the ceria surface. Our previous work [44] has proved that manganese species on the ceria surface shows multiple oxidation states, which may improve the reducibility of catalysts for the faster electron transfer processes [35]. The surface M/Cu atomic ratio of CuC–Fe catalyst is only 0.01, which means almost all of iron ions incorporate into the ceria lattice instead of being distributed on the ceria surface. This also means that the shrinkage of the lattice parameter is mainly caused by the incorporation of iron ions. However, CuC–Co catalyst has the highest Cu content and very little of Co content on the surface, which may suggest that copper ions in ceria lattice are replaced by cobalt ions and then segregated from the lattice to aggregate on the ceria surface (Fig. 6).

The oxidation states of Ce are also analyzed by fitting the curves of Ce 3d spectra obtained from XPS measurements. As shown in Fig. 7, the curves of Ce 3d spectra are composed of eight peaks corresponding to four pairs of spin-orbit doublets [47]. The proportion of Ce<sup>3+</sup> ions with regard to the total cerium is calculated from the ratio of the sum of areas of the Ce<sup>3+</sup> species to the sum

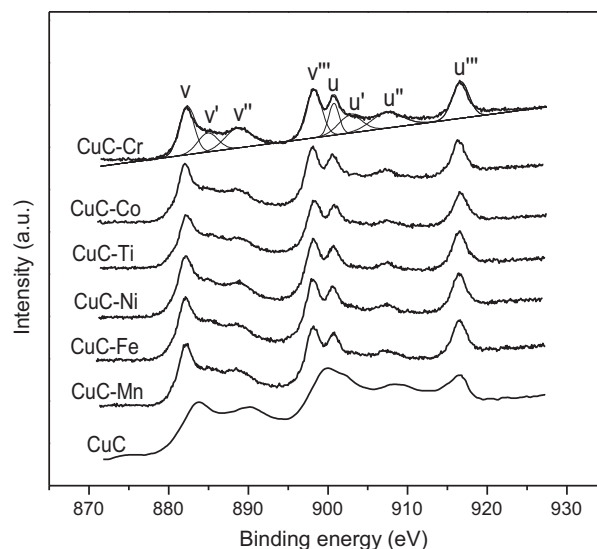


**Fig. 6.** Ce 3d XPS spectra for CuO–CeO<sub>2</sub> catalysts doped with transition metals.

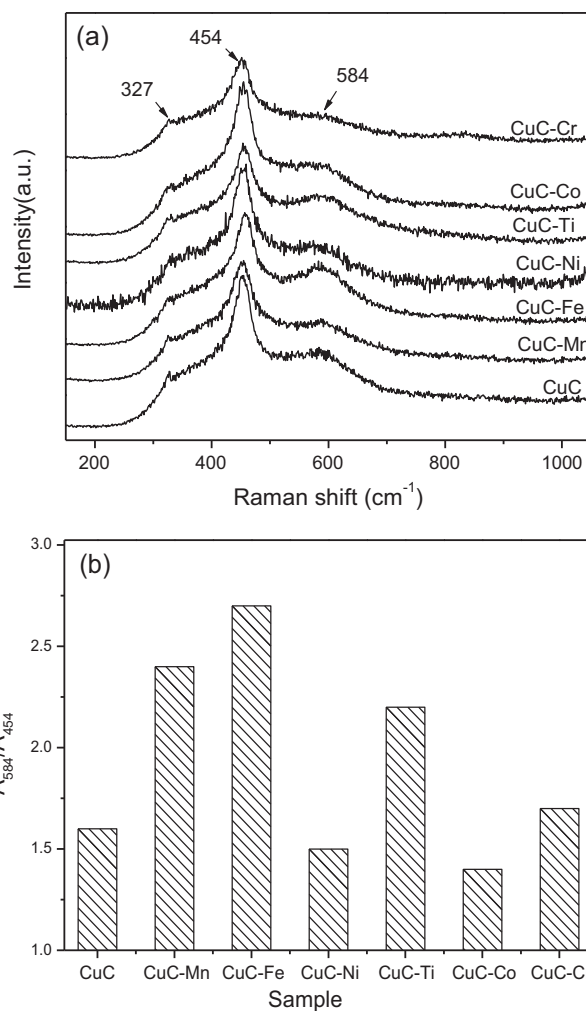


**Fig. 7.** UV–Raman patterns (a) and the  $A_{584}/A_{454}$  ratio (b) of CuO–CeO<sub>2</sub> catalysts doped with transition metals.

of areas of the total cerium species [47]. The relative concentration of  $\text{Ce}^{3+} 3d_{5/2}$  in Ce is obtained in Table 2 in the sequence of  $\text{CuC-Mn} > \text{CuC-Fe} > \text{CuC-Ti} > \text{CuC} > \text{CuC-Ni} > \text{CuC-Co} > \text{CuC-Cr}$ . It is known that the presence of  $\text{Ce}^{3+}$  is associated with the formation of oxygen vacancies [47,48]. Therefore, the addition of Mn, Fe and Ti favors the reduction of  $\text{Ce}^{4+}$  to  $\text{Ce}^{3+}$  and/or the formation of oxygen vacancy, which may lead  $\text{CuO-CeO}_2$  catalyst to exhibit higher activity for selective oxidation of CO. The decrease of the  $\text{Ce}^{3+}$  content caused by the introduction of Ni, Co and Cr may be correlated to the increased crystallite size of  $\text{CeO}_2$ , inasmuch as the larger crystallite size corresponds to the smaller concentration of exposed  $\text{Ce}^{3+}$  and the resultant oxygen vacancies [48].

### 3.2.5. UV-Raman

Raman spectroscopy was used to study the lattice structure for its sensitivity to both M–O bond arrangement and lattice defects, and the corresponding spectra of  $\text{CuO-CeO}_2$  catalysts doped with different transition metals are shown in Fig. 7(a). No obvious shifts in the band position are noted. All catalysts maintain a cubic phase in respect that a strong peak at  $454\text{ cm}^{-1}$ , corresponding to the  $\text{F}_{2g}$  Raman vibration mode of the cubic fluorite-structure phase [47,49], is observed. In addition to  $\text{F}_{2g}$ -like contribution, two new bands are observed for the samples at  $584$  and  $327\text{ cm}^{-1}$ , respectively. The broad band at  $584\text{ cm}^{-1}$  corresponds to non-degenerate LO mode of ceria due to relaxation of symmetry rules, which is often linked to oxygen vacancies in the ceria lattice according to McBride et al. [49]. The other weak band at  $327\text{ cm}^{-1}$  could be attributed to the displacement of oxygen atoms from their ideal fluorite lattice positions [50]. No Raman lines attributed to copper oxide or dopant oxides could be observed owing to the incorporation of copper and dopants into the ceria lattice. Furthermore, the central locations of strong bands deviate from the  $465\text{ cm}^{-1}$  of the pure  $\text{CeO}_2$  [49], which also indicate that copper and dopant ions incorporate into the ceria lattice to form solid solution. This is because the incorporated ions into the ceria lattice will induce the lattice to distort, which will influence the polarizability of the symmetrical stretching mode of  $[\text{Ce-O}_8]$  vibrational unit and result in the shift from that in the pure  $\text{CeO}_2$  [51]. These results are in agreement with the analysis results of XRD that a solid solution is formed. Besides, according to the literature [52], the relative concentration of oxygen vacancies in the solid solution can be represented by the area ratio of peaks  $584$  and  $454\text{ cm}^{-1}$  (noted as  $A_{584}/A_{454}$ ), and the calculated results are depicted in Fig. 7(b). The ratios of  $A_{584}/A_{454}$  is on the order of  $\text{CuC-Fe} > \text{CuC-Mn} > \text{CuC-Ti} > \text{CuC-Cr} > \text{CuC} > \text{CuC-Ni} > \text{CuC-Co}$ , indicating that the introduction of Mn, Fe and Ti increases the amount of oxygen vacancies in the ceria lattice. The reaction mechanism of CO oxidation on  $\text{CeO}_2$  is considered to be a redox reaction involving lattice oxygen and oxygen vacancies. Based on the results of both XPS and UV-Raman, one can deduce that the increasing of the lattice oxygen and oxygen vacancies will be conducive to CO oxidation. However, the decreasing amount of oxygen vacancies, induced by the addition of Ni and Co, may be because the presence of Ni and Co inhibits the substitutional incorporation of copper ions into the ceria lattice, which must be accompanied by the generation of oxygen vacancies ( $\text{Ce}^{4+} + \text{O}^{2-} \leftrightarrow \text{Cu}^{2+} + \text{V}_\text{O}$ ;  $\text{V}_\text{O}$  being a doubly ionized oxygen vacancy) [53].

### 3.2.6. In situ DRIFTS

DRIFTS experiments recorded under the simple  $\text{CO} + \text{O}_2 + \text{H}_2$  reaction stream are displayed in Figs. 8–9. Bands formed under such a reactant stream are observed to be basically present in three distinct zones of wavenumber in the spectra. The first zone in the  $3800\text{--}2650\text{ cm}^{-1}$  (not shown) displays bands mostly corresponding to the hydroxyl species. These include isolated hydroxyls and associated species [54,55]. A second zone below  $1750\text{ cm}^{-1}$

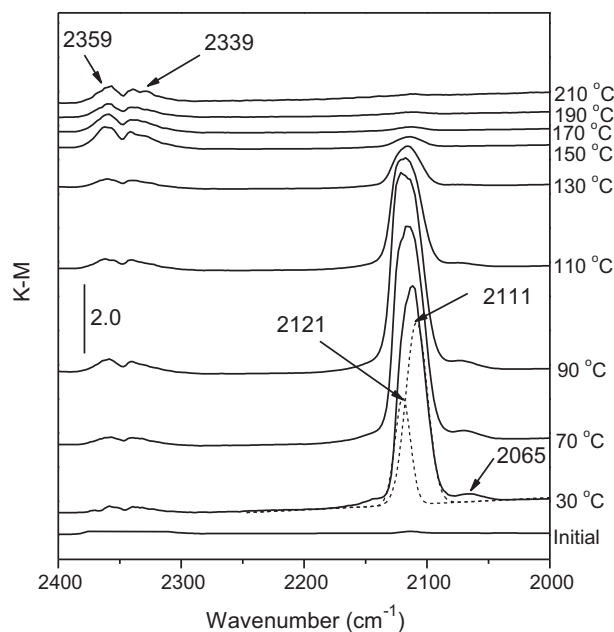


**Fig. 8.** DRIFTS spectra of  $\text{CuO-CeO}_2$  catalyst recorded under the simple  $\text{CO} + \text{O}_2 + \text{H}_2$  reaction stream. An indicated in the right part, the bottom spectrum corresponds to the initial one prior to introduction of the reactant stream; the rest corresponds to spectra recorded every  $20^\circ\text{C}$  from  $30^\circ\text{C}$  to  $210^\circ\text{C}$ , from bottom to top.

(not shown) exhibits bands ascribed to carbonate, carboxylate or formate species [56]. Two above mentioned spectra zones of  $\text{CuO-CeO}_2$  catalysts doped with different transition metals show little difference with those of  $\text{CuO-CeO}_2$  catalyst.

The other zone in the  $2400\text{--}2000\text{ cm}^{-1}$  shows the formation of  $\text{CO}_2$  (g) (the two rotational branches at  $2359$  and  $2339\text{ cm}^{-1}$ , evolving in accordance with CO oxidation activity [36]) and carbonyl species (stretching region at  $2200\text{--}2000\text{ cm}^{-1}$ ). For  $\text{CuO-CeO}_2$  catalyst, as shown in Fig. 8, there are multiple bands appearing in the  $2200\text{--}2000\text{ cm}^{-1}$ , revealing that there is a spontaneous variation in the extent reduction of  $\text{CuO-CeO}_2$  at room temperature. As detailed in previous contributions [36,56,57], for the  $\text{Cu}^{n+}\text{-CO}$  system, regions of  $2200\text{--}2140\text{ cm}^{-1}$ ,  $2140\text{--}2100\text{ cm}^{-1}$  and  $2100\text{--}2000\text{ cm}^{-1}$  are typical for CO adsorption on  $\text{Cu}^{2+}$ ,  $\text{Cu}^+$  and  $\text{Cu}^0$  sites, respectively. Moreover,  $\text{Cu}^{2+}\text{-CO}$  species is unstable and can be disregarded at room temperature [58]. The low-frequency band at  $2065\text{ cm}^{-1}$  is attributed to CO adsorption at small metallic copper clusters [59]. The high-frequency bands at  $2130\text{--}2110\text{ cm}^{-1}$  are considered to be due to CO adsorption at  $\text{Cu}^+$  sites, considering that  $\text{Cu}^+\text{-CO}$  species detected on pure  $\text{Cu}_2\text{O}$  gives a main IR adsorption band at about  $2127\text{ cm}^{-1}$  [60] and the interaction between copper and ceria can make the band shift to the red according to previous contributions [27,36,56,61]. In addition, the attribution of adsorption center to  $\text{Cu}^+$  instead of metallic copper atoms is in agreement with their significantly high thermal stability [27]. The presence of these  $\text{Cu}^+\text{-CO}$  species is consistent with the easy reduction copper in the catalysts, in agreement with the results of  $\text{H}_2\text{-TPR}$  experiments (Fig. 5). As shown in Fig. 8, two bands corresponding to  $\text{Cu}^+\text{-carbonyls}$  appear at  $2111\text{ cm}^{-1}$  and  $2121\text{ cm}^{-1}$ . It is known that the relatively low frequency of these bands with respect to those expected for  $\text{Cu}^+$  carbonyls has been related to the interaction between those copper centers and the underlying ceria, suggesting a  $\pi$ -back-bond component in them, within the common  $\sigma$  bond- $\pi$  back-bond scheme adopted to explain carbonyl bonds in this type of species [60,62]. The lower frequency of  $\text{Cu}^+\text{-carbonyl}$  at  $2111\text{ cm}^{-1}$  than that at  $2121\text{ cm}^{-1}$  implies the presence of a stronger M–C bond and a weaker C–O bond [62], which reflects in a stronger red shift of the C–O stretching vibration and may be due to that partial copper

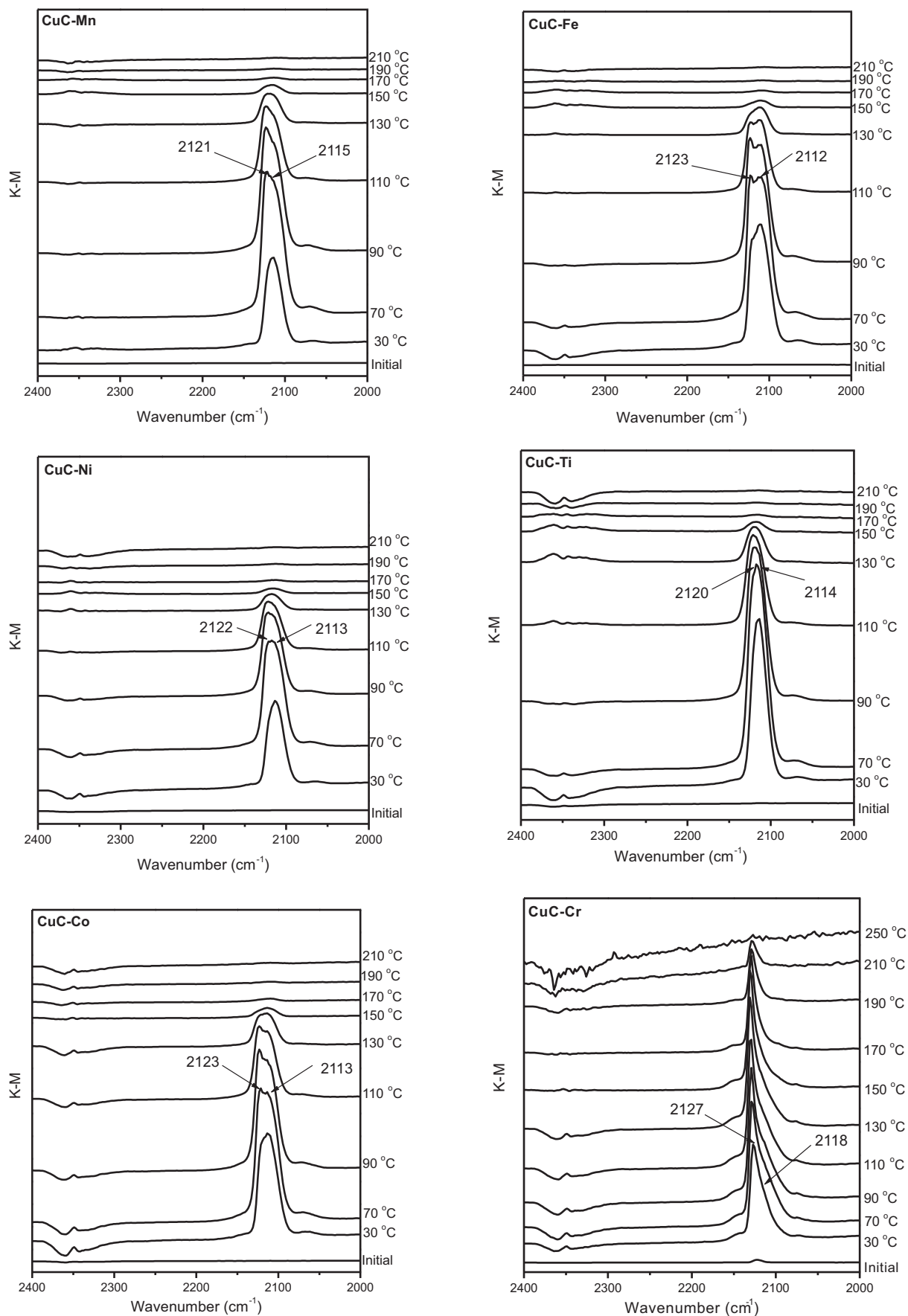


**Fig. 9.** DRIFTS spectra of CuO-CeO<sub>2</sub> catalyst doped with transition metals recorded under the simple CO + O<sub>2</sub> + H<sub>2</sub> reaction stream. As indicated in the right part, the bottom spectrum corresponds to the initial one prior to introduction of the reactant stream; the rest corresponds to spectra recorded every 20 °C from 30 °C to 210 °C, from bottom to top.

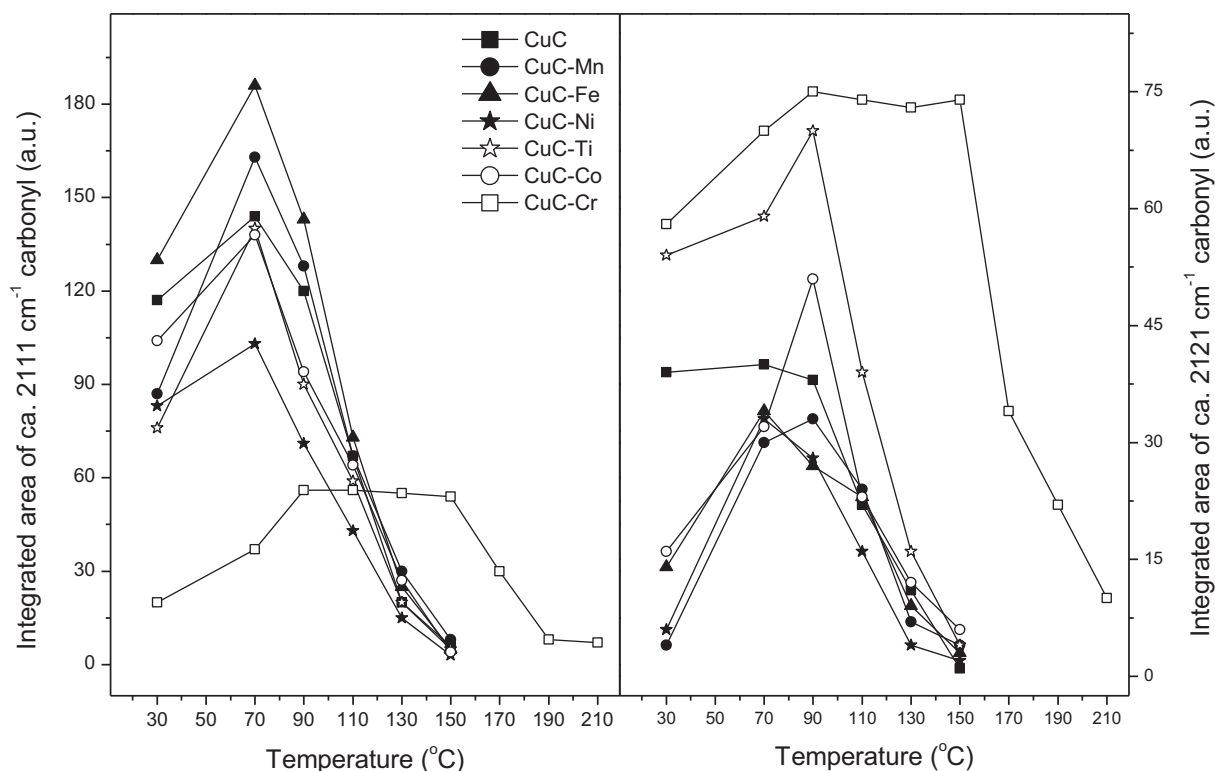


Fig. 10. Intensity of the  $\text{Cu}^+$ -carbonyls as a function of reaction temperature under the indicated  $\text{CO} + \text{O}_2 + \text{H}_2$  reaction mixtures.

oxides are likely to have a stronger interaction with the ceria support [36,61]. Therefore,  $\text{Cu}^+$ -carbonyl at  $2111\text{ cm}^{-1}$  is related to the copper species exhibiting a stronger interaction with ceria while that at  $2121\text{ cm}^{-1}$  is related to the isolated copper species on the ceria surface and/or copper species possessing a weaker interaction with ceria.

For  $\text{CuO-CeO}_2$  catalyst, the intensity of two bands at  $2111\text{ cm}^{-1}$  and  $2121\text{ cm}^{-1}$  first increases and then reaches a maximum at  $70^\circ\text{C}$ . With further increasing the reaction temperature, these two peaks are weakened and completely disappear at  $170^\circ\text{C}$ . The same phenomenon occurs on the  $\text{CuO-CeO}_2$  catalysts doped with different transition metals. As shown in Fig. 9, the bands at  $2111\text{ cm}^{-1}$  and  $2121\text{ cm}^{-1}$  slightly shift to higher wavenumber in the presence of different transition metals, suggesting a lower influence of Cu-Ce interaction on the red shift of  $\text{Cu}^+$ -carbonyls frequency. Moreover, for CuC-Cr catalyst, the bands of  $\text{Cu}^+$ -carbonyls at  $2118\text{ cm}^{-1}$  and  $2127\text{ cm}^{-1}$  possesses the maximum degree of blue shift, indicating  $\pi$ -back-bond component responsible for the red shift would be seriously hindered by the presence of Cr in the sample. The fact also means CuC-Cr catalyst shows the weakest interaction between copper and ceria, which is in good agreement with the  $\text{H}_2$ -TPR results. In addition, as reported in literature [27], the intensity of these bands is correlated to the CO oxidation activity of the catalysts. To further investigate the relationship between two  $\text{Cu}^+$ -carbonyls and catalytic activity for CO selective oxidation in  $\text{H}_2$ -rich streams, evolution of the intensity of two  $\text{Cu}^+$ -carbonyls with the reaction temperature is displayed in Fig. 10. The sequence of the intensity of band at  $2111\text{ cm}^{-1}$  is  $\text{CuC-Fe} > \text{CuC-Mn} > \text{CuC} > \text{CuC-Ti} \approx \text{CuC-Co} > \text{CuC-Ni} > \text{CuC-Cr}$ , while that of band at  $2121\text{ cm}^{-1}$  is  $\text{CuC-Cr} > \text{CuC-Ti} > \text{CuC-Co} > \text{CuC} > \text{CuC-Fe} \approx \text{CuC-Ni} \approx \text{CuC-Mn}$ . Obviously, the variation of the intensity of band at  $2111\text{ cm}^{-1}$  is basically consistent with that of catalytic activity, whereas that of band at  $2121\text{ cm}^{-1}$  is contrary to the catalytic activity, which indicates that a strong interaction between copper and ceria favors

catalytic activity for CO selective oxidation. CuC-Cr catalyst shows the largest integrated area of band at  $2121\text{ cm}^{-1}$  and the smallest integrated area of band at  $2111\text{ cm}^{-1}$ , which may be the most important reason for the poor catalytic performance of CuC-Cr catalyst.

#### 4. Conclusions

In this work,  $\text{CuO-CeO}_2$  catalysts doped by different transition metals (Mn, Fe, Ni, Ti, Co and Cr) were prepared by hydrothermal method. The catalytic activity for selective oxidation of CO in  $\text{H}_2$ -rich streams follows the sequence of  $\text{CuC-Mn} \approx \text{CuC-Fe} > \text{CuC-Ti} > \text{CuC-Ni} > \text{CuC} > \text{CuC-Co} > \text{CuC-Cr}$ .

CuC-Mn catalyst exhibits the widest temperature window, about  $40^\circ\text{C}$ , from  $110$  to  $140^\circ\text{C}$ . CuC-Fe catalyst has the best low-temperature catalytic activity. The superior catalytic performance of CuC-Mn and CuC-Fe catalysts originates from the enhanced interaction between copper and ceria, owing to the formation of more  $\text{Cu}^+$  and oxygen vacancies in the solid solution framework. The doping of Ni and Ti promotes the catalytic activity to a certain extent, according to the wider temperature windows of  $30^\circ\text{C}$ , from  $120$  to  $140^\circ\text{C}$  for CuC-Ti and CuC-Ni catalysts. However, the introduction of Co and Cr inhibits the catalytic activity of  $\text{CuO-CeO}_2$  for selective oxidation of CO. The results of XRD and XPS show that the poor catalytic activity of CuC-Co catalyst is mainly ascribed to the substitution of introduced cobalt ions for copper ions in ceria lattice, resulting in the segregation of copper ions from the lattice and the consequent aggregation on the ceria surface. The results of  $\text{H}_2$ -TPR and DRIFTS analysis indicate that the introduction of Cr into  $\text{CuO-CeO}_2$  catalyst greatly weakens the interaction between copper and ceria. The weakened interaction decreases the reducibility of copper species and inhibits the formation of  $\text{Cu}^+$ , which accounts for the lowest catalytic performance of CuC-Cr catalyst for selective oxidation of CO in  $\text{H}_2$ -rich streams.



## Acknowledgements

We gratefully acknowledge the financial support from the Ministry of Science and Technology of China (No. 2011AA03A406) as well as Science and Technology Department of Zhejiang Province (No. 2009R50020).

## Appendix A. Supplementary data

Supplementary data associated with this article can be found, in the online version, at [doi:10.1016/j.apcatb.2011.08.010](https://doi.org/10.1016/j.apcatb.2011.08.010).

## References

- [1] X. Yu, H. Li, S.-T. Tu, J. Yan, Z. Wang, *Int. J. Hydrogen Energy* 36 (2011) 3778–3788.
- [2] Q. Zhang, X. Liu, F. Qing, Y. Wang, *Appl. Catal. B: Environ.* 102 (2011) 207–214.
- [3] G. Sedmak, S. Hocevar, J. Levec, *J. Catal.* 213 (2003) 135–150.
- [4] J.W. Park, J.H. Jeong, W.L. Yoon, C.S. Kim, D.K. Lee, Y. Park, Y.W. Rhee, *Int. J. Hydrogen Energy* 30 (2005) 209–220.
- [5] Q. Guo, Y. Liu, *Appl. Catal. B: Environ.* 82 (2008) 19–26.
- [6] N. Bion, F. Epron, M. Moreno, F. Mariño, D. Duprez, *Top. Catal.* 51 (2008) 76–88.
- [7] C.G. Maciel, L.P.R. Profeti, E.M. Assaf, J.M. Assaf, *J. Power Sources* 196 (2011) 747–753.
- [8] C. Pedrero, T. Waku, E. Iglesia, *J. Catal.* 233 (2005) 242–255.
- [9] J.L. Ayastuy, M.P. Gonzalez-Marcos, J.R. Gonzalez-Velasco, M.A. Gutierrez-Ortiz, *Appl. Catal. B: Environ.* 70 (2007) 532–541.
- [10] F. Marino, C. Descorme, D. Duprez, *Appl. Catal. B: Environ.* 54 (2004) 59–66.
- [11] R.J.H. Grisel, B.E. Nieuwenhuys, *J. Catal.* 199 (2001) 48–59.
- [12] B. Schumacher, Y. Denkwitz, V. Plzak, M. Kinne, R.J. Behm, *J. Catal.* 224 (2004) 449–462.
- [13] F. Arena, P. Famulari, G. Trunfio, G. Bonura, F. Frusteri, L. Spadaro, *Appl. Catal. B: Environ.* 66 (2006) 81–91.
- [14] C.G. Maciel, M.N. Belgacem, J.M. Assaf, *Catal. Lett.* 141 (2011) 316–321.
- [15] F. Mariño, G. Baronetti, M. Laborde, N. Bion, A.L. Valant, F. Epron, D. Duprez, *Int. J. Hydrogen Energy* 33 (2008) 1345–1353.
- [16] J.-Y. Luo, M. Meng, X. Li, X.-G. Li, Y.-Q. Zha, T.-D. Hu, Y.-N. Xie, J. Zhang, *J. Catal.* 254 (2008) 310–324.
- [17] J. Han, H.J. Kim, S. Yoon, H. Lee, *J. Mol. Catal. A: Chem.* 335 (2011) 82–88.
- [18] G. Avgouropoulos, T. Ioannides, Ch. Papadopolou, J. Batista, S. Hocevar, H.K. Matralis, *Catal. Today* 75 (2002) 157–167.
- [19] C.R. Jung, A. Kundu, S.W. Nam, H.-I. Lee, *Appl. Catal. B: Environ.* 84 (2008) 426–432.
- [20] G. Avgouropoulos, T. Ioannides, *Appl. Catal. B: Environ.* 67 (2006) 1–11.
- [21] G. Avgouropoulos, T. Ioannides, H. Matralis, *Appl. Catal. B: Environ.* 56 (2005) 87–93.
- [22] X. Zheng, X. Zhang, X. Wang, S. Wang, S. Wu, *Appl. Catal. A: Gen.* 295 (2005) 142–149.
- [23] G. Avgouropoulos, T. Ioannides, *Appl. Catal. A: Gen.* 244 (2003) 155–167.
- [24] M.-F. Luo, J.-M. Ma, J.-Q. Lu, Y.-P. Song, Y.-J. Wang, *J. Catal.* 246 (2007) 52–59.
- [25] A. Gómez-Cortés, Y. Márquez, J. Arenas-Alatorre, G. Díaz, *Catal. Today* 133–135 (2008) 743–749.
- [26] C.R. Jung, J. Han, S.W. Nam, T.-H. Lim, S.-A. Hong, H.-I. Lee, *Catal. Today* 93–95 (2004) 183–190.
- [27] D. Gamarra, C. Belver, M. Fernández-García, A. Martínez-Arias, *J. Am. Chem. Soc.* 129 (2007) 12064–12065.
- [28] Y.-Z. Chen, B.-J. Liaw, H.-C. Chen, *Int. J. Hydrogen Energy* 31 (2006) 427–435.
- [29] Y.-Z. Chen, B.-J. Liaw, W.-C. Chang, C.-T. Huang, *Int. J. Hydrogen Energy* 32 (2007) 4550–4558.
- [30] T.-J. Huang, Y.-C. Kung, *Catal. Lett.* 85 (2003) 49–55.
- [31] J. Chen, J. Zhu, Y. Zhan, X. Lin, G. Cai, K. Wei, Q. Zheng, *Appl. Catal. A: Gen.* 363 (2009) 208–215.
- [32] C.R. Jung, A. Kundu, S.W. Nam, H.-I. Lee, *Appl. Catal. A: Gen.* 331 (2007) 112–120.
- [33] Z. Wu, H. Zhu, Z. Qin, H. Wang, L. Huang, J. Wang, *Appl. Catal. B: Environ.* 98 (2010) 204–212.
- [34] T.H. Etsell, S.N. Flengas, *Chem. Rev.* 70 (1970) 339–376.
- [35] X. Wu, Q. Liang, D. Weng, J. Fan, R. Ran, *Catal. Today* 126 (2007) 430–435.
- [36] D. Gamarra, A. Martínez-Arias, *J. Catal.* 263 (2009) 189–195.
- [37] F. Mariño, C. Descorme, D. Duprez, *Appl. Catal. B: Environ.* 58 (2005) 175–183.
- [38] B. Coasne, A. Grosman, C. Ortega, M. Simon, *Phys. Rev. Lett.* 88 (2002) 256102.
- [39] X. Du, Z. Yuan, L. Cao, C. Zhang, S. Wang, *Fuel Process. Technol.* 89 (2008) 131–138.
- [40] T. Baidya, A. Gayen, M.S. Hegde, N. Ravishanker, L. Dupont, *J. Phys. Chem. B* 110 (2006) 5262–5272.
- [41] X. Zhu, H. Wang, Y. Wei, K. Li, X. Cheng, *J. Rare Earths* 28 (2010) 907–913.
- [42] W. Shan, M. Luo, P. Ying, W. Shen, C. Li, *Appl. Catal. A: Gen.* 246 (2003) 1–9.
- [43] H. Liu, L. Wei, R. Yue, Y. Chen, *Catal. Commun.* 11 (2010) 829–833.
- [44] J. Li, P. Zhu, S. Zuo, Q. Huang, R. Zhou, *Appl. Catal. A: Gen.* 381 (2010) 261–266.
- [45] P. Zhu, J. Li, S. Zuo, R. Zhou, *Appl. Surf. Sci.* 255 (2008) 2903–2909.
- [46] W. Liu, M. Flytzani-Stephanopoulos, *J. Catal.* 153 (1995) 317–332.
- [47] J. Fan, X. Wu, X. Wu, Q. Liang, R. Ran, D. Weng, *Appl. Catal. B: Environ.* 81 (2008) 38–48.
- [48] P. Dutta, S. Pal, M.S. Seehra, Y. Shi, E.M. Eyring, R.D. Ernst, *Chem. Mater.* 18 (2006) 5144–5146.
- [49] J.R. McBride, K.C. Hass, B.D. Poindexter, W.H. Weber, *J. Appl. Phys.* 76 (1994) 2435–2441.
- [50] H. Vidal, J. Kašpar, M. Pijolat, G. Colon, S. Bernal, A. Cordon, V. Perrichon, F. Fally, *Appl. Catal. B: Environ.* 27 (2000) 49–63.
- [51] Y. She, Q. Zheng, L. Li, Y. Zhan, C. Chen, Y. Zheng, X. Lin, *Int. J. Hydrogen Energy* 34 (2009) 8929–8936.
- [52] Z.-Y. Pu, J.-Q. Lu, M.-F. Luo, Y.-L. Xie, *J. Phys. Chem. C* 111 (2007) 18695–18702.
- [53] D. Gamarra, G. Munuera, A.B. Hungria, M. Fernández-García, J.C. Conesa, P.A. Midgley, X.Q. Wang, J.C. Hanson, J.A. Rodríguez, A. Martínez-Arias, *J. Phys. Chem. C* 111 (2007) 11026–11038.
- [54] A. Badri, C. Binet, J.-C. Lavalley, *J. Chem. Soc. Faraday Trans.* 92 (1996) 4669–4673.
- [55] C. Binet, M. Daturi, J.-C. Lavalley, *Catal. Today* 50 (1999) 207–225.
- [56] A. Hornés, P. Bera, A.L. Cámara, D. Gamarra, G. Munuera, A. Martínez-Arias, *J. Catal.* 268 (2009) 367–375.
- [57] M. Manzoli, R.D. Monte, F. Boccuzzi, S. Coluccia, J. Kašpar, *Appl. Catal. B: Environ.* 61 (2005) 192–205.
- [58] R. Kydd, D. Ferri, P. Hug, J. Scott, W.Y. Teoh, R. Ama, *J. Catal.* 277 (2011) 64–71.
- [59] F. Boccuzzi, G. Ghiotti, A. Chiorino, *Surf. Sci.* 162 (1985) 361–367.
- [60] D. Scarano, S. Bordiga, C. Lamberti, G. Spoto, G. Ricchiardi, A. Zecchina, C. Otero Areán, *Surf. Sci.* 411 (1998) 272–285.
- [61] P. Bera, A.L. Cámara, A. Hornés, A. Martínez-Arias, *J. Phys. Chem. C* 113 (2009) 10689–10695.
- [62] K.I. Hadjiivanov, M.M. Kantcheva, D.G. Klissurski, *J. Chem. Soc. Faraday Trans.* 92 (1996) 4595–4600.